


Inhibiting the onset of thermoacoustic instability through targeted control of critical regions

International Journal of Spray and Combustion Dynamics
2023, Vol. 15(1) 3–15
© The Author(s) 2023
Article reuse guidelines:
sagepub.com/journals-permissions
DOI: 10.1177/17568277221149507
journals.sagepub.com/home/scd



Manikandan Raghunathan¹ , Nitin Babu George^{2,4,*},
Vishnu R. Unni³, Jürgen Kurths^{2,4}, Elena Surovyatkina^{2,5}
and R. I. Sujith¹

Abstract

This experimental study investigates the dynamical transition from stable operation to thermoacoustic instability in a turbulent bluff-body stabilised dump combustor. We conduct experiments to acquire acoustic pressure and local heat release rate fluctuations and use them to characterise this transition as we decrease the equivalence ratio towards a fuel-lean setting. More importantly, we observe a significant increase in local heat release rate fluctuations at critical locations well before thermoacoustic instability occurs. One of these critical locations is the stagnation zone in front of the bluff-body. By strategically positioning slots (perforations) on the bluff-body, we ensure the reduction of the growth of local heat release rate fluctuations at the stagnation zone near the bluff-body well before the onset of thermoacoustic instability. We show that this reduction in local heat release rate fluctuations inhibits the transition to thermoacoustic instability. We find that modified configurations of the bluff-body that do not quench the local heat release rate fluctuations at the stagnation zone result in the transition to thermoacoustic instability. We also reveal that an effective suppression strategy based on the growth of local heat release rate fluctuations requires an optimisation of the slots' area-ratio for a given bluff-body position. Further, the suppression strategy also depends on the spatial distribution of perforations on the bluff-body. Notably, an inappropriate distribution of the slots, which does not quench the local heat release rate fluctuations at the stagnation zone but creates new critical regions, may even result in a dramatic increase in the amplitudes of pressure oscillations.

Keywords

Thermoacoustic instability, critical transition, suppression

Date received: 29 June 2022; accepted: 16 December 2022

Introduction

The catastrophic onset of thermoacoustic instability has been a challenging barrier in developing low-emission propulsion and power generation systems. Thermoacoustic instability, which manifests as high amplitude periodic pressure and heat release rate oscillations, causes structural failure and overwhelms the thermal protection system.^{1,2} Thus, investigating the onset of the transition, which is a regime change from chaotic dynamics to limit cycle oscillations^{3,4} and mitigating its occurrence has gained substantial scientific interest in the past decades.

Two main control strategies exist for mitigating thermoacoustic instability: active and passive control. Active control relies on external energy sources employing actuators to keep the combustor from deviating significantly from a desired operating state.⁵ Unlike active control methods, passive control strategies seek to alter the

fundamental dynamics of the combustion system and break the mutually enhancing interactions between unsteady heat release rate and chamber acoustics.^{6–8} In recent decades, studies have shown that mitigation of

¹Department of Aerospace Engineering, Indian Institute of Technology Madras, Chennai, India

²Potsdam Institute for Climate Impact Research, Potsdam, Germany

³Department of Mechanical and Aerospace Engineering, Indian Institute of Technology Hyderabad, Hyderabad, India

⁴Department of Physics, Humboldt University of Berlin, Berlin, Germany

⁵Space Research Institute of Russian Academy of Sciences, Moscow, Russia

*Contributed equally.

Corresponding author:

Manikandan Raghunathan, Department of Aerospace Engineering, Indian Institute of Technology Madras, 600036, India.
Email: manikandanraghu05@gmail.com

thermoacoustic instability is possible by modifying the spatiotemporal dynamics of the flame/flow through injection of secondary air/fuel.^{9–12} In another type of passive control method, the linear growth rate of oscillations around the base flow is forced to be negative. Aguilar and Juniper¹³ employ a simple network model with sensitivity analysis to comprehend the dynamics of the combustor during thermoacoustic stability. They reported that variations in the base flow must be taken into account in the same manner as variations in the fluctuating flow. Tammisola and Juniper¹⁴ proved that, despite the swirl combustor's complicated mean flow structure, the region of dominant coherent structures upstream of the central recirculation zone is dynamically significant for the self-sustained thermoacoustic oscillations. Many passive control strategies are based on suppressing the visible large-scale patterns, such as large-scale coherent structures and standing waves that characterise thermoacoustic instability.^{15–17} However, such large-scale patterns may appear well after the transition to thermoacoustic instability has occurred.

Traditionally, the onset of thermoacoustic instability in turbulent combustors has been considered as a sudden transition in the system dynamics wherein the system behaviour shifts from stable operation (refer as combustion noise) to unstable operation (refer as thermoacoustic instability).¹⁸ However, Nair et al.¹⁹ have shown that in a turbulent combustor, the transition is not abrupt, but instead occurs through a state of intermittency, wherein bursts of periodic oscillations occur amidst aperiodic oscillations.

Various spatiotemporal patterns distinguish combustion noise, intermittency and thermoacoustic instability. The characteristics of combustion noise are disorganised flow and flame dynamics^{20–22} and chaotic acoustic pressure fluctuations.^{3,4} Macroscopic patterns at the size of the system geometry emerge during the regime of periodic oscillations, whereas disordered small-scale structures exist during the regime of aperiodic oscillations during the state of intermittency.^{20–22}

Thermoacoustic instability, on the other hand, is characterised by the coexistence of large-scale coherent flow structures or vortices⁷ and spatially organised reaction fields.²¹ During the transition from combustion noise to thermoacoustic instability via intermittency, the disordered dynamics decrease while the ordered dynamics increase due to the collective behaviour of small-scale structures.^{21,22}

Measures based on pressure fluctuations derived from recurrence plots and multifractality have shown early detection of the impending onset of thermoacoustic instability.^{23–27} Similarly, measures based on spatial patterns of flame fluctuations such as spatial correlation also indicate the impending onset of thermoacoustic instability.^{21,28–30} These temporal and spatial-based measures change well before the appearance of the large-scale spatial or large-amplitude temporal patterns, which suggests that the signature of the impending transition to

thermoacoustic instability appears much earlier. Therefore, preventing the transition to thermoacoustic instability requires suppressing the onset of the transition itself, which occurs far ahead of large-scale patterns that appear during thermoacoustic instability.

In spatially extended systems such as turbulent combustors, it is very difficult to control the transitions due to the possibility of diverse unstable modes that may exist in the system. A spatially extended system is a system with a large number of spatially distributed degrees of freedom, where spatial distribution or spatial inhomogeneity plays a significant role in determining the system's dynamics.³¹ The turbulent combustor displays a spatially heterogeneous distribution of heat release rates, which influences the system's combustion process. Moreover, a turbulent combustor exhibits distinct spatiotemporal patterns under various operating circumstances, which is another characteristic of spatially extended systems.

Consider the Rayleigh-Bénard convection system, a well-studied spatially extended system with different modes of instabilities and associated patterns.³² In the Rayleigh-Bénard convection system, the range of Rayleigh numbers Ra and Prandtl numbers Pr determines the spatial patterns that form.^{33,34} A control scheme that is based on controlling a specific unstable mode at certain operating conditions does not guarantee that it will maintain the system's stability under other operating conditions, because of alternate routes to different modes of instability in spatially extended systems. For example, Parekh and Sinha³⁵ uses external perturbations in a spatially extended two-coupled map lattice system to control both the local and global dynamics towards being stable or unstable depending on the strength and sign of the perturbation. They demonstrated that perturbation with the opposite sign does not always result in a stable state, but rather enhances an unstable state due to the spatially inhomogeneous or spatially extended nature of the system, where the local dynamics are regulated by coupled processes of multiple variables, and hence the control strategy depends crucially on the variable perturbed.

The turbulent thermoacoustic system is one such spatially extended system with multiple spatiotemporal patterns coexisting under different operating conditions, that is, different equivalence ratios or Reynolds numbers and different experimental configurations. George et al.³⁶ demonstrated that the transition to thermoacoustic instability in a turbulent combustor may be prevented by decreasing the growth of local heat release rate fluctuations in the stagnation zone by introducing slots on the bluff body. In this study, we explore this strategy further by varying the locations of these slots and checking the effectiveness of the strategy under different operating conditions and experimental configurations to analyse the impact of the spatially extended nature of the turbulent flame. In particular, we find that certain arrangements of the slots introduce new

spatiotemporal patterns of the heat release rate, which do not suppress the transition to thermoacoustic instability. Thus, an effective control strategy utilizing slotted bluff bodies requires an optimisation of the slot distribution to suppress thermoacoustic instability and ensure that new critical regions are not formed.

Experimental setup

We perform experiments in a bluff-body stabilised turbulent dump combustor, as shown in Figure 1(a). Air enters through the plenum chamber while fuel enters and mixes with air just before the burner, resulting in partially pre-mixed reactants. In all our experiments, we use Liquefied Petroleum Gas (LPG) as the fuel. The flame is stabilised using a bluff-body, which is a circular disk of 47 mm diameter and 10 mm thickness. The cross-section of the combustion chamber is 90 mm \times 90 mm with a combustor length of 1100 mm. We perform experiments at different bluff-body positions from the dump plane: 40 and 45 mm.

The fuel and air supply to the combustor are controlled using Alicat mass flow controllers (MFCs) which have an uncertainty \pm (0.8% of the reading + 0.2% of the full scale). We perform experiments at different mass flow rate of fuel (\dot{m}_{fuel}) and different rates of change of mass flow rate of air (\dot{m}_{air}). For each experiment, we control the equivalence ratio (ϕ) by maintaining \dot{m}_{fuel} constant and continuously vary \dot{m}_{air} . We control \dot{m}_{air} by utilizing an NI DAQ. More details regarding the system are given in Raghunathan et al.³⁷ The lowest and highest values of the Reynolds number in our experiments are $1.28 \times 10^4 \pm 345$ and $2.47 \times 10^4 \pm 594$, respectively.

We vary ϕ from 0.99 to 0.56 and simultaneously acquire experimental data. For all the experiments, we record temporal signals of acoustic pressure and the global heat release rate at a sampling rate of 10 kHz by using an A/D card

(NI-6143, 16 bit). The acoustic pressure signals were acquired using a piezoelectric pressure transducer (PCB103B02, uncertainty \pm 0.15 Pa) that is mounted at a distance of 25 mm from the dump plane of the combustor. The pressure transducer is fixed with a T-joint and inserted into a Teflon adaptor. The addition of the T-joint mount and adaptor results in a maximum amplitude error of \pm 12% and a phase difference of 5° for the frequency range of 50–1000 Hz. In addition, the uncertainty is smaller, that is, \pm 2% and 2° in the range of the dominant frequencies used in our experiments (100–200 Hz). As a result, these variations in the amplitude of pressure oscillations or the phase difference do not affect our analysis significantly. We measure the global heat release rate fluctuations in the flame with a photomultiplier tube (PMT, Hamamatsu H10722-01) equipped with a CH* filter (wavelength of 430 nm and 12 nm FWHM). For selected experiments, we acquire spatially resolved high-speed CH* chemiluminescence images of the flame using a CMOS camera (Phantom-v12.1) at a sampling rate of 500 fps and a spatial resolution of 800 \times 600 pixels. The camera was equipped with a ZEISS 50 mm camera lens at $f/2$ aperture outfitted with a CH* filter (wavelength of 430 nm and 12 nm FWHM).

Phase transition in turbulent thermoacoustic systems

In a recent study, Raghunathan et al.³⁷ analysed the transition to thermoacoustic instability in a turbulent combustor as a phase transition. A phase transition is the commencement of nontrivial macroscopic behaviour in a system made up of a large number of constituents that obey simple microscopic principles. In the theory of phase transition, it is widely known that for a given system, if a relevant control parameter is adjusted and pushed close to its critical threshold, the system will demonstrate a significant

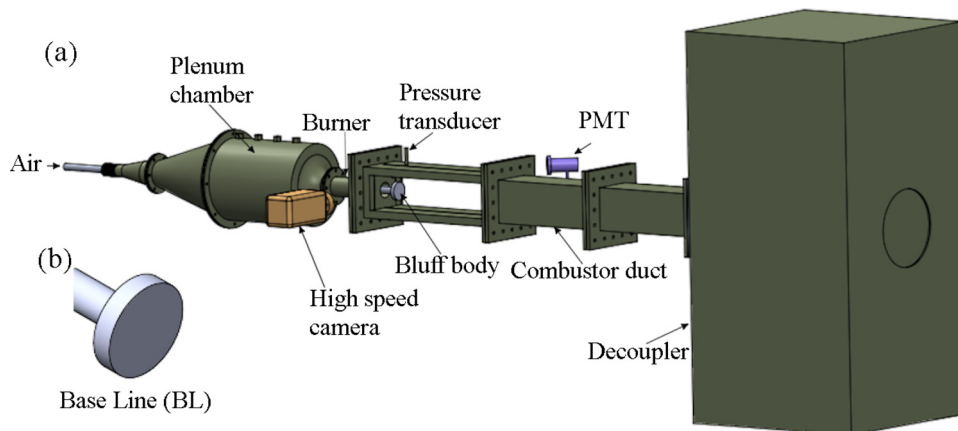


Figure 1. Schematic diagram of the experimental setup used in this study. (a) The main components of the setup are a plenum chamber, a combustion duct and a decoupler. The data acquisition system comprises of a piezoelectric pressure transducer, a photomultiplier tube and a high-speed camera. (b) Schematic diagram of the baseline (BL) bluff-body.

qualitative shift in its macroscopic features. Such a shift may appear as regularities in spatiotemporal behaviour as disordered patterns change to self-organised patterns.^{38–40} In a turbulent thermoacoustic system, considering the transition to thermoacoustic instability as a phase transition is justified because the transition occurs between two qualitatively dissimilar states. The first state is characterised by disordered spatiotemporal dynamics, while the state of thermoacoustic instability has ordered spatiotemporal dynamics.

As the control parameter approaches the critical point, the initial stable state loses its stability and, concurrently, the damping decreases and becomes zero at the critical point, resulting in a growth of fluctuations in state variable near the phase transition. The increase in critical fluctuations before the critical point can be interpreted as an indicator of impending phase transitions. Recently, Raghunathan et al.³⁷ showed early local growth of flame fluctuations prior to the critical transition to the onset of thermoacoustic instability.

We compute the variance of fluctuations σ^2 of the local heat release rate ($\dot{q}(x, y, t)$) at each pixel for a time period of window size $w = 3.5$ s, where the fluctuations are computed using a moving average of $w_s = 0.04$ s. d denotes the time at which the calculation is conducted.

$$\sigma^2(\dot{q}, d, w, w_s) = \sum_{k=1}^w \frac{\left[\dot{q}(OOD - d - k) - \frac{\sum_{i=1}^{w_s} \dot{q}(OOD - d - k - i)}{w_s} \right]^2}{w} \quad (1)$$

For example, assuming OOD is at 25 s, to calculate σ^2 20 s (d) before the OOD , we utilise the fluctuations from $t = 1.5$ s to $t = 5$ s. OOD is the onset of ordered dynamics, which is defined as the reference time instant at which the first derivative of the phase difference ($\delta\theta$) between the acoustic pressure and the global heat release rate ($\frac{d\delta\theta}{dt}$) achieves 99.99% of the greatest positive value and zero.

The window size w is chosen such that the entire flame dynamics are captured during the transition from one state to another. For example, the window size should be sufficient and large enough to capture both the aperiodic and periodic epochs during the state of intermittency. As a result, a window size w of 3.5 s works well in this analysis. Similarly, a window size greater than 3.5 s is incapable of capturing this increase in the variance of fluctuations. The value of w_s is based on the time scales of acoustic oscillations during thermoacoustic instability. Given the dominating frequency of acoustic pressure, we require at least four cycles of data for the moving average window size (w_s) in order to calculate any fluctuations-based measures.²⁷ As a result, for a dominant frequency of 150 Hz, the moving average window size w_s was determined to be equivalent to six cycles, or 0.04 s. Appendix E of Raghunathan et al.³⁷ demonstrates that, for the provided window sizes, the increase in σ^2 is 99.9% significant using the student t -test.

In particular, Raghunathan et al.³⁷ revealed significant growth of local heat release rate fluctuations occurring at certain zones within the combustor, located around the bluff-body. Additionally, they revealed interconnections that emerged between these zones prior to the transition to thermoacoustic instability.

Results and discussion

Characterisation of the phase transition at different operating conditions

To begin with, we analyse the results from an experiment in which the combustor length was set to 1100 mm and the bluff-body was fixed at a distance of 45 mm from the dump plane, with operating settings, including a \dot{m}_{fuel} of 34 SLPM and a \dot{m}_{air} change at a rate of 3 SLPM/s. We refer to this set of operating settings and experimental configurations utilised in Raghunathan et al.³⁷ as the reference experimental condition (REC) for the purpose of comparing results across different operating settings and different bluff bodies. For all the subsequent figures, instead of discussing the plots with respect to \dot{m}_{air} , we describe the figures using the global equivalence ratio ϕ . Even though the flame is only partially premixed, we use ϕ so that we can compare the results at different thermal power ratings.

The acoustic pressure (p') and global heat release rate oscillations (\dot{Q}') as a function of ϕ for the BL bluff-body at reference experimental condition are depicted in Figure 2(a). Figure 2(a) shows that the amplitudes of p' and \dot{Q}' increase continuously as ϕ decreases. In order to detrend the signal, \dot{Q}' is computed about the mean of a sliding window of size, 0.04 s. The short-time Fourier transform (STFT) plot in Figure 2(b) shows a dominant mode of p' emerging near 100 Hz at $\phi < 0.87$. As ϕ is reduced, the frequency of the dominant mode increases and reaches an asymptotic state for $\phi < 0.67$. At high values of ϕ ($0.99 \geq \phi \geq 0.88$), p' and \dot{Q}' have dissimilar dominant modes with shallow bands.⁴¹

Next, we analyse how the root mean square of heat release rate fluctuations $\dot{q}'(x, y, t)$ varies with ϕ . Here, CH^* chemiluminescence intensity (I_{CH^*}) is used as a measure for the localised heat release rate. Numerous investigations have demonstrated that the I_{CH^*} can be approximated as the rate of heat release in partially premixed flames.^{42,43} Additionally, we found a strong correlation between the normalised global heat release rate measured by the PMT and the normalised integral of I_{CH^*} obtained from images at various ϕ . This high correlation suggests that the change in dynamics in \dot{Q}' is represented well by I_{CH^*} in the experiments (significant correlation p value = 0.86). The spatial distribution of the root mean square value of the local heat release rate fluctuations \dot{q}'_{rms} is shown at three values of equivalence ratio, $\phi = 0.97$ (Figure 2(c)), $\phi = 0.88$ (Figure 2(d)) and $\phi = 0.69$

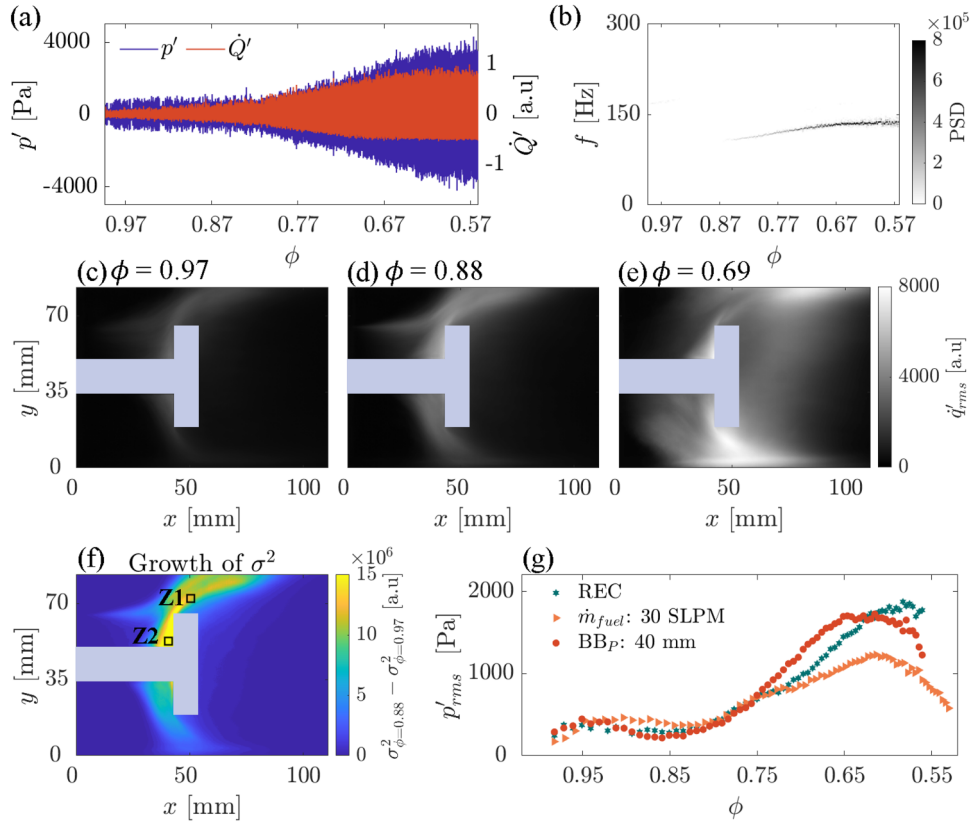


Figure 2. Spatiotemporal dynamics with respect to the transition from combustion noise to thermoacoustic instability for the BL bluff-body at REC. The term ‘Reference Experimental Condition’ (REC) refers to experimental settings where the experiments are carried out at $\dot{m}_{fuel} = 34$ SLPM with a \dot{m}_{air} change at a rate of 3 SLPM/s with fixing a combustor length as 1100 mm and a bluff-body (BB_p) located 45 mm away from the dump plane. (a) Time series of pressure oscillations p' and global heat release rate fluctuations \dot{Q}' with respect to ϕ . (b) Evolution of power spectral density obtained using the STFT of p' . \dot{q}'_{rms} at (c) $\phi = 0.97$, (d) $\phi = 0.88$ and (e) $\phi = 0.69$. (f) Growth of σ^2 calculated as $\sigma^2_{\phi=0.88} - \sigma^2_{\phi=0.97}$. (g) Variation in p'_{rms} for different operating conditions and combustor configurations as stated in the legend. BL: baseline; STFT: short-time Fourier transform.

(Figure 2(e)). We calculate the mean using a window size of 1 s corresponding to 500 images. Given a maximum dominant frequency of 150 Hz and the time scale of the rate of change of operating parameter, a window size of 1 s is sufficient to demonstrate the variation in \dot{q}'_{rms} as ϕ changes. \dot{q}'_{rms} shows high strength around the bluff body and near the combustor walls.

According to the phase transition theory,⁴⁴ at the approaching critical threshold, the initial state of the system is losing its stability, and small perturbations lead to a strong fluctuation response and a longer return to equilibrium, indicated by an increase in signal variance and autocorrelation. Such a nonlinear behaviour appearing in the vicinity of a critical threshold has the collective name ‘the critical phenomena’. In particular, the phenomenon of pre-bifurcation noise amplification followed by saturation indicates upcoming instability that is measured by the variance of fluctuations (σ^2) of observable variables.⁴⁵ In our investigation, the critical phenomenon was characterised by an increase in the variance of fluctuations in

the heat release rate. We estimate the growth of σ^2 of the local heat release rate fluctuations from the difference between σ^2 at $\phi = 0.97$ and $\phi = 0.88$ (Figure 2(f)). We use these two values of ϕ (also for subsequent sections) to calculate the growth of σ^2 prior to the occurrence of large-amplitude pressure oscillations (refer Figure 2(a)) for the REC.

According to the phase transition theory, critical phenomena occur at approaching a phase transition. In the context of phase transition, critical phenomena are regarded as an increase in the variance of fluctuations of system variables, an increase in autocorrelation, etc. In particular, the phenomenon of pre-bifurcation noise amplification followed by saturation⁴⁵ indicates upcoming instability that is measured by the variance of fluctuations (σ^2) of observable variables. In our investigation, the critical phenomenon is characterised by an increase in the variance of fluctuations in the heat release rate. We estimate the growth of σ^2 of the local heat release rate fluctuations from the difference between σ^2 at $\phi = 0.97$ and $\phi = 0.88$ (Figure 2(f)).

We use these two values of ϕ (also for subsequent sections) to calculate the growth of σ^2 prior to the occurrence of large-amplitude pressure oscillations (refer Figure 2(a)) for the REC.

We mark two regions, Z1 and Z2, that have high growth of σ^2 using black squares in Figure 2(f). Z1 is a location of the high heat release rate during the occurrence of thermoacoustic instability because of the impingement of large-scale coherent flow structures on the combustor wall. Z1 is a zone shared by the boundaries of the large-scale coherent structures that emerge from the dump plane and vortices that emerge at the tip of the bluff-body. Z2 represents a stagnation point that stabilises the flame because of the low-velocity region at the corner between the shaft and the bluff-body. Both Z1 and Z2 exhibit critical phenomena prior to the transition to thermoacoustic instability, illustrated by the high growth in σ^2 (Figure 2(f)). In our previous study,³⁷ we referred to these zones as ‘seeds’ of the phase transition due to critical phenomena occurring at these locations, well before the appearance of large-amplitude pressure oscillations. After the critical transition in the local heat release rate fluctuations occurs at these zones, the strength of pressure oscillations (p'_{rms}) increases rapidly as ϕ is reduced for REC as shown in Figure 2(g).

We now analyse the effect of change in bluff-body position and \dot{m}_{fuel} on the transition to thermoacoustic instability. We show p'_{rms} in Figure 2(g) for the case where the position of bluff-body is fixed at 40 mm from the dump plane keeping the other operating settings are the same. From Figure 2(g), it appears that large-amplitude oscillations occur earlier compared to that of 45 mm bluff-body (REC). However, at $\phi < 0.6$, the pressure oscillations with 45 mm bluff-body position (REC) is stronger than those with 40 mm.

We also investigate changes in the transition with respect to the thermal power rating: \dot{m}_{fuel} . We reduced \dot{m}_{fuel} to 30 SLPM, and acquired acoustic pressure from $\phi = 0.99$ to 0.55. We see from Figure 2(g), that p'_{rms} for $\dot{m}_{fuel} = 30$ SLPM is followed the similar trends like REC till $\phi = 0.7$. For $\phi < 0.7$, p'_{rms} is lower in comparison to REC.

In an earlier study, George et al.³⁶ targeted one of these interconnected zones, namely the stagnation zone upstream of the bluff-body by introducing the slots in the bluff-body. They show that reducing the growth of local heat release rate fluctuations at the stagnation zone resulted in the suppression of the transition to thermoacoustic instability. In this study, we take the next step and change the operating conditions and bluff body designs to analyse the effectiveness of the control strategy on the spatially extended system.

Reducing the growth of fluctuations at the stagnation zone near the bluff-body and suppressing the transition to thermoacoustic instability

We use a modified design of the bluff-body to create additional passages for the fluid to flow across the bluff-body.³⁶

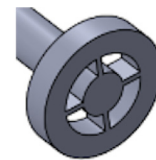
We create four slots near the region attached to the shaft as depicted in Figure 3. We refer to this configuration as the inner slot (IS) bluff-body. In this IS bluff-body geometry, in addition to demonstrating the suppression strategy for REC, we also show how the position of the bluff-body impacts the effectiveness of the control technique.

The high growth in σ^2 at the boundary of the large-coherent structure that is shed from the bluff-body tip, Z1, and at the stagnation zone near the bluff-body, Z2 (see Figure 2(f)) occurs under all of the operating conditions described in the section on system characterisation in the presence of the BL bluff-body. In the current parametric study on the suppression of the phase transition to thermoacoustic instability, we will target the stagnation zone and modify the flame distribution around the bluff-body.

Utilizing the IS bluff-body design, we introduce passages on the bluff-body in the form of slots. These slots are introduced between a radius of 8 and 15 mm. Since the shaft radius is also 8 mm, we eliminate the stagnation zone at the corner between the bluff-body and the shaft in order to reduce the growth of local heat release rate fluctuations at the stagnation zone. We first analyse results with the IS bluff-body at REC.

Figure 4(a) to (c) shows the variation in the spatial distribution of \dot{q}'_{rms} as the equivalence ratio is reduced. The IS configuration results in higher strength of the local heat release rate oscillations downstream of the bluff-body (see Figure 4(b) and (c)) in comparison to the BL configuration. In comparison to the BL bluff-body at REC, we observe that the strength of the heat release rate oscillations (\dot{q}'_{rms}) have reduced at the stagnation point (refer Figures 2(d) and (e) and 4(b) and (c)). The highest strength of \dot{q}' oscillations are observed near the combustor walls (see Figure 4(c)).

Thus, the IS bluff-body design redistributes the heat release rate fluctuations around the bluff-body. This redistribution results in a reduction of growth of σ^2 at the stagnation zone (Figure 4(d)). This low growth corresponds with a reduction of \dot{q}'_{rms} at the stagnation zone. On the other hand, near the boundary of the downstream large-scale coherent flow structure, the growth of σ^2 is still high. Further, the wake region of the IS bluff-body also indicates a growth of σ^2 . But importantly, the growth of σ^2 is not as high as the growth at the stagnation zone.



Inner Slot (IS)

Figure 3. Schematic diagram of the bluff-body with slots near the centre – inner slot (IS) bluff-body.

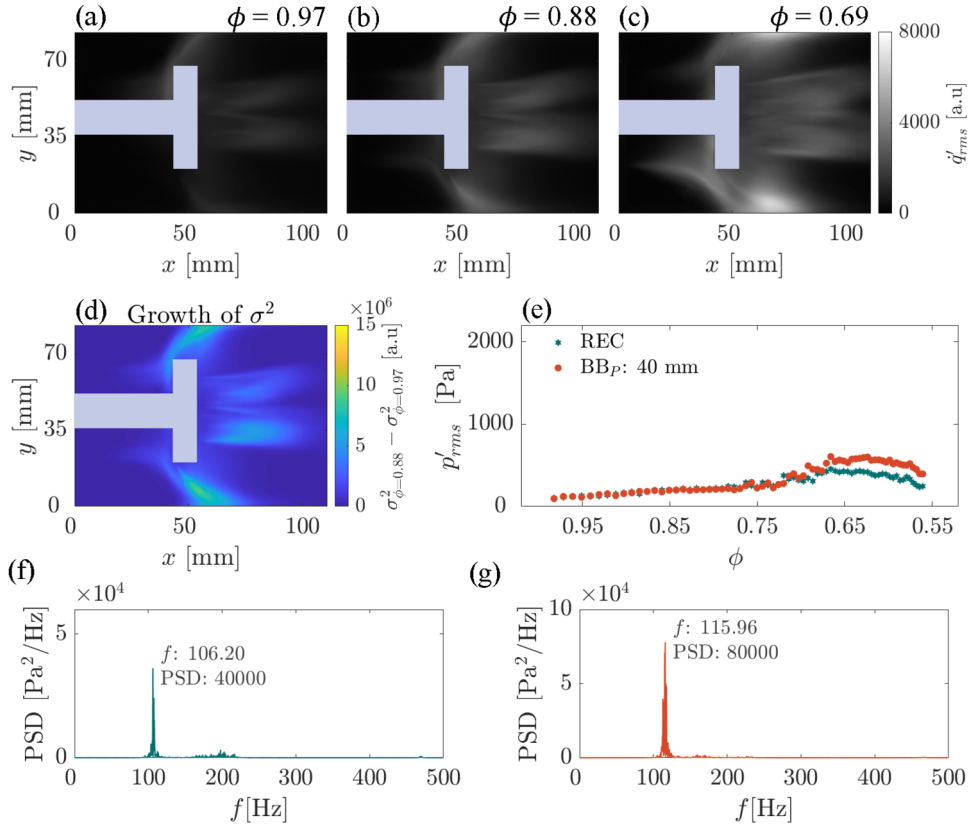


Figure 4. Spatiotemporal dynamics for experiments conducted utilizing the IS bluff-body. \dot{q}'_{rms} at (a) $\phi = 0.97$, (b) $\phi = 0.88$ and (c) $\phi = 0.69$ for REC. (d) Growth of σ^2 : $\sigma^2_{\phi=0.88} - \sigma^2_{\phi=0.97}$ for REC. (e) p'_{rms} for different operating conditions and combustor configurations with respect to ϕ . Power spectral density of p' for (f) REC, (g) BB_p : 40 mm. REC: Reference Experimental Condition; IS: inner slot.

It is crucial that other regions do not show high growth of σ^2 due to the change in the bluff-body design. Other regions showing high growth of σ^2 may mean the existence of other pathways for the transition to thermoacoustic instability.

The plot of p'_{rms} at REC shows the suppression of the global transition to thermoacoustic instability (Figure 4(e)). p'_{rms} remains low as ϕ is reduced to low values. In fact, at low values of ϕ , there is 88% decrease in the rms value of pressure oscillations in comparison to the rms value obtained with BL bluff-body at REC. However, p'_{rms} at low values of ϕ with IS bluff-body is 0.45 kPa that is approximately 21% higher than the strength of pressure oscillations ($p'_{rms} = 0.37$ kPa) at high values of ϕ (combustion noise) with the BL bluff-body. The power spectral density of p' for REC at $\phi = 0.69$ shows a shallow band centred around 106.2 Hz (Figure 4(f)). This dominant mode obtained using IS bluff-body at REC is 17.4 Hz less than the dominant mode observed for the BL bluff-body at REC.

Irrespective of the changes in the thermal power loading (\dot{m}_{fuel}), there is a suppression of thermoacoustic instability when the IS bluff-body is used (shown in Supplemental Figure 10). However, a higher reduction of the strength of pressure oscillations is observed for higher \dot{m}_{fuel} .

In addition, as the bluff-body is brought closer to the dump plane from 45 to 40 mm, the maximum strength of pressure oscillations decreases by 77% compared to the case with the BL bluff-body at 40 mm. This decrease in pressure oscillations is not as large as the one seen with a 45 mm bluff-body position (see Figure 4(e)). For this bluff-body position of 40 mm, the PSD of p' at $\phi = 0.69$ displayed in Figure 4(g) shows a shallow band centred around 116 Hz, which is higher when compared to the band corresponding to REC with IS bluff-body. However, this frequency is still lower than the narrow band (123.6 Hz) observed for REC with BL bluff-body (refer Figure 2(b)).

Effect of reducing the area of the slots on the bluff-body

We investigate the effect of changes in the area of the passage by the four-hole (4H) bluff-body. In this design, we create circular holes near the region that is attached to the shaft (Figure 5(a)). The total area of these four circular holes is 113 mm², which is a quarter of the total area of the slots on the IS bluff-body. We use the design with the reduced area to investigate minimum area requirements of the slots to suppress the transition to

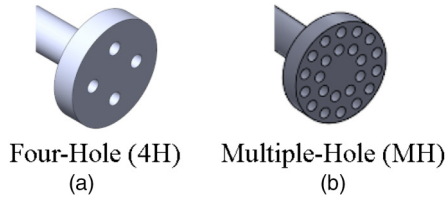


Figure 5. Schematic diagram of the different bluff-bodies. (a) Four-hole (4H) bluff-body is a bluff-body with four holes near the centre. (b) Multiple holes of diameter 5 mm are distributed around the bluff-body, referred to as the multiple-hole (MH) bluff-body.

thermoacoustic instability. Analysis of the local heat release rate fluctuations prove that for the 4H bluff-body, near the boundary of the downstream large-scale coherent flow structure, and at the stagnation zone, (i) higher \dot{q}'_{rms} exists compared to IS bluff-body (Figure 6(a) to (c)) and (ii) high growth of σ^2 occurs (Figure 6(d)). In addition, we observe a small growth of σ^2 in the wake of the 4H bluff-body due to secondary flames, as observed with the IS bluff-body.

When comparing the experimental results at REC between 4H and BL bluff bodies, we do not observe any large changes in the transition from low-amplitude pressure fluctuations to high-amplitude pressure oscillations (Figure 6(e)). A gradual growth in p'_{rms} occurs when using REC (Figure 6(e)). The strength of p' at low ϕ is also similar in magnitude with the strength obtained for BL bluff-body. However, the power spectral density of p' at $\phi = 0.69$ shows a sharp peak centred around 115.7 Hz (Figure 6(f)), which is significantly lower than the frequency of the dominant mode observed with the BL bluff-body (123.6 Hz) (Figure 2(b)) for the same combustor length. From the results obtained with the 4H bluff-body, it is evident that the introduction of slots has shifted the dominant frequency to a lower value for the experiments performed at REC. Thus, a new temporal pattern has emerged in the combustor at thermoacoustic instability.

When operating at a higher rate of change of \dot{m}_{air} , the change in the transition is negligible in comparison to the p'_{rms} for REC (Figure 6(e)). The dominant frequency at $\phi = 0.69$ is 114.7 Hz (Figure 6(g)). Thus, multiple experiments with the 4H bluff-body show that the onset of thermoacoustic instability is not suppressed due to the emergence of a new unstable mode in the combustor. The reduction in the amplitude of pressure oscillations for the 4H configuration is negligible with respect to the BL bluff-body.

Effect of change in the distribution of the bluff-body passage area

We now investigate the effect of change in the distribution of the passages on the bluff-body. To that end, we utilise the

multiple-hole (MH) bluff-body. This design contains twenty-three circular holes of diameter 5 mm, distributed over the bluff-body as shown in Figure 5(b). The total area of these circular holes is same as the total area of the slots in the IS bluff-body. In Figure 7(a) to (c), we observe high strength of \dot{q}'_{rms} near the boundary of the downstream large-scale coherent flow structure, and downstream of the MH bluff body for REC. As shown in Figure 7(d), with the MH bluff-body, the growth of σ^2 still exists at the stagnation zone, although it is low. Higher growth of σ^2 downstream of the bluff-body can be attributed to the large heat release rate fluctuations of the multiple secondary flames anchored on the bluff-body surface.

Using the MH bluff-body, we observe a similar transition from combustion noise to thermoacoustic instability to that of BL bluff body till $\phi = 0.75$ (refer Figures 2(g) and 7(e)). The p'_{rms} with MH bluff-body for REC (679 Pa) is slightly higher compared to the p'_{rms} obtained with the BL bluff-body at REC (644 Pa). The power spectral density of p' at $\phi = 0.69$ show the dominant frequency at 128 Hz (Figure 7(f)). This dominant frequency is marginally greater than the dominant frequency obtained with the BL bluff-body (123.6 Hz) (Figure 2(b)), but closest to it as compared to the values obtained with IS and 4H bluff bodies. Thus, suppression of the transition does not occur for the MH bluff-body.

Interestingly, as the equivalence ratio is reduced further to less than 0.66, an additional very sharp transition occurs as shown in Figure 7(e). The increase in the strength of pressure oscillations is rather catastrophic, increasing to almost 300% of the p'_{rms} value after the primary transition. Such a secondary transition is referred to as a secondary bifurcation.⁴⁶ The occurrence of high-amplitude limit cycles through secondary bifurcation may be attributed to the presence of higher-order nonlinearities in the system.⁴⁷ The dominant frequency increases to 150 Hz for the secondary bifurcation at $\phi = 0.62$ (Figure 7(g)).

As the thermoacoustic system is spatially extended, the occurrence of the secondary bifurcation through the use of the MH bluff body is not surprising. The spatial and temporal patterns after the primary transition and the secondary transition are different, as observed by the shift in dominant frequencies from 128 to 150 Hz and changes in the spatial pattern of the local heat release rate. The various spatial and temporal modes that exist within the spatially extended system is the reason why preventing the transition to thermoacoustic instability is challenging. Any control strategy that is employed should ensure that it does not create alternate pathways for thermoacoustic instability to emerge through conducive spatiotemporal patterns. In the case of the MH bluff-body, the highest growth of local heat release rate fluctuations is not observed at the stagnation point, but rather downstream of the bluff-body as a result of the secondary flames (Figure 7(h)). The appearance of

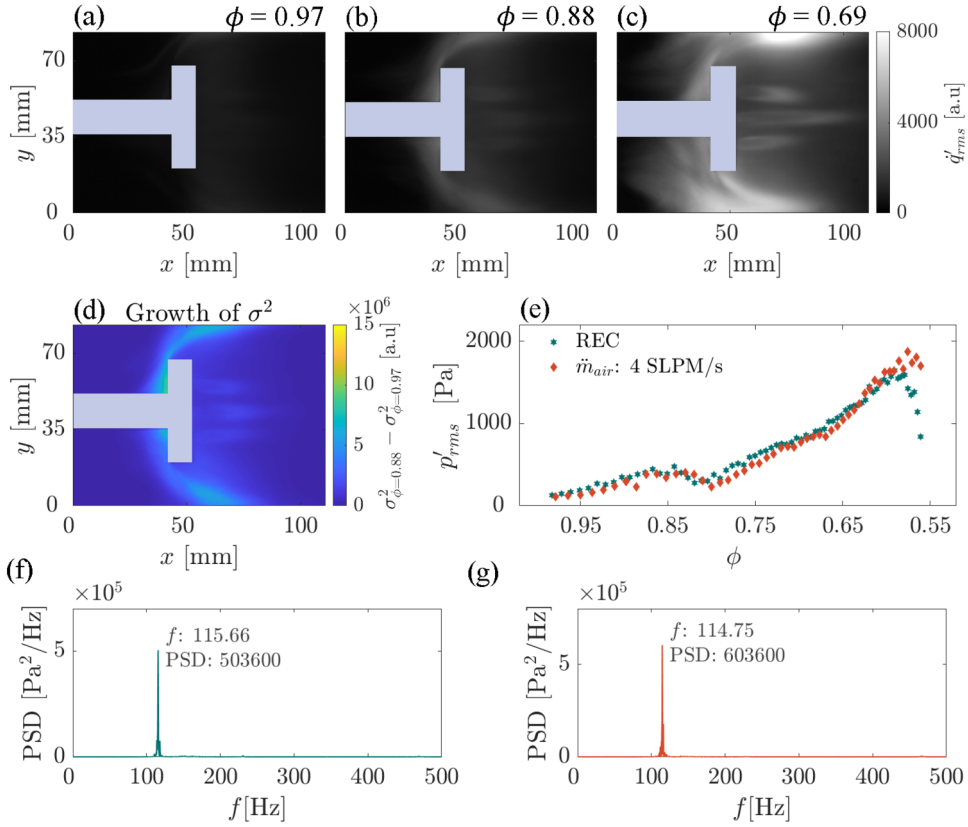


Figure 6. Spatiotemporal dynamics for experiments conducted using the 4H bluff-body at REC. \dot{q}'_{rms} at (a) $\phi = 0.97$, (b) $\phi = 0.88$ and (c) $\phi = 0.69$. Growth of σ^2 : $\sigma^2_{\phi_2} - \sigma^2_{\phi_1}$. p'_{rms} for different operating conditions and combustor configurations with respect to ϕ . Power spectral density of p' for (f) REC, (g) rate of change of mass flow rate of air: $\dot{m}_{air} = 4$ SLPM/s. 4H: four-hole; REC: Reference Experimental Condition.

new regions with high growth of heat release rate fluctuations shows the existence of alternative pathways to thermoacoustic instability.

In summary, we devised a control strategy based on the suppression of critical phenomena occurring in the key regions of the combustor. As one of the approaches to achieving the target of suppression of critical phenomena, we redesigned the three bluff-bodies, namely IS, 4H, and MH. With the modified designs, we observe that, apart from the flame stabilisation zone upstream of the bluff-body, the flame gets an additional zone downstream to stabilise there. However, it is interesting to see that the suppression of thermoacoustic instability is seen only in one bluff-body geometry, whereas in the other two geometries, either the thermoacoustic instability is retained or the system goes to a new state of thermoacoustic instability. In addition to looking into the flame stabilisation point, we have ensured that the critical phenomenon is suppressed and that there is also no formation of new regions of critical phenomenon. In that context, IS bluff-body serves this purpose, whereas the other two bluff-body geometries do not. Thus, in the reduction of thermoacoustic instability, the IS bluff-body geometry is therefore recommended over other bluff-body geometries.

Change in Rayleigh index distribution for different bluff-body geometries

We observe diverse forms of thermoacoustic instability with different bluff-body geometries, indicating that the process by which net energy is transferred from combustion to the acoustic field may be distinct. The Rayleigh Index, RI offers substantial insight into combustion dynamics and the mechanisms that lead to thermoacoustic instabilities.⁴⁸ The RI is calculated as

$$RI = \frac{1}{T} \int_1^T p'(t) \dot{q}'(x, y, t) dt. \quad (2)$$

where $p'(t)$ denotes the acoustic pressure fluctuation, $\dot{q}'(x, y, t)$ is the local heat release rate fluctuations, T is the time period taken for the analysis and t is the variable over which integration is performed. RI denotes if the flame-acoustic interaction is driving thermoacoustic instability or not. A positive value shows that the flame-acoustic interaction results in thermoacoustic driving while a negative value indicates damping. The RI field for BL bluff-body geometry evaluated at $\phi = 0.69$ for the REC is depicted in Figure 8(a). The RI field shows which regions drive and

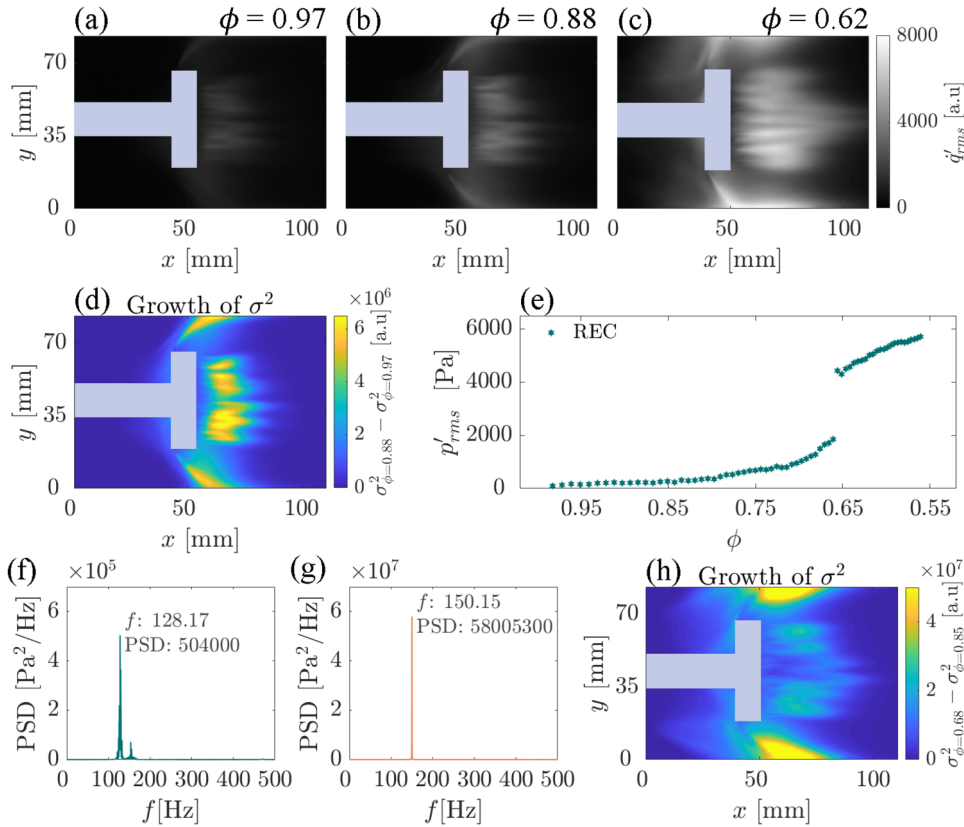


Figure 7. Spatiotemporal dynamics for experiments conducted utilizing the MH bluff-body at REC. q'_{rms} at (a) $\phi = 0.97$, (b) $\phi = 0.88$ and (c) $\phi = 0.62$. (d) Growth of σ^2 for the primary bifurcation: $\sigma^2_{\phi=0.88} - \sigma^2_{\phi=0.97}$. (e) p'_{rms} with respect to ϕ for REC. Power spectral density of p' for (f) primary bifurcation at $\phi = 0.69$ and (g) secondary bifurcation at $\phi = 0.62$. (h) Growth of σ^2 for secondary bifurcation: $\sigma^2_{\phi=0.68} - \sigma^2_{\phi=0.75}$. REC: Reference Experimental Condition; MH: multiple-hole.

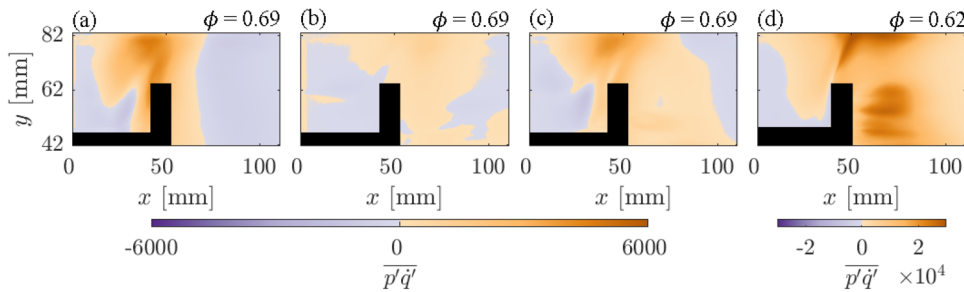


Figure 8. At $\phi = 0.69$, the Rayleigh index RI maps for (a) BL, (b) IS and (c) 4H bluff-bodies are shown. (d) RI map for the MH bluff body at $\phi = 0.62$ is shown. The spatial mean of positive RI values, RIM , indicates the strength of the acoustic power driving the thermoacoustic oscillations. The order of strength of acoustic power is $RIM_{MH} > RIM_{BL} > RIM_{4H} > RIM_{IS}$, which results in strong pressure oscillations. BL: baseline; IS: inner slot; 4H: four-hole; MH: multiple-hole.

damp thermoacoustic instability. Figure 8(a) to (d) shows the RI field for BL, IS, 4H and MH, respectively. For the BL bluff-body, the region with the highest positive RI coincides with Z1.

For the IS bluff-body, the positive RI region is extended out and shifted more downstream, which is caused by the presence of secondary flame downstream of the bluff body. In the case of 4H bluff-body geometry, the RI field exhibits

interesting characteristics, namely, the positive RI is observed in Z1, and downstream of the bluff-body. As in the BL bluff-body geometry, the maximum positive RI value occurs around Z1, although with a smaller magnitude than the maximum RI value found for the BL bluff-body geometry.

We estimate RI for MH bluff-body at $\phi = 0.62$, where the MH bluff-body shows a single peak in the amplitude spectra (refer Figure 7(g)). In the case of MH bluff-body, the region

of positive RI extends from the bluff-body's upstream to the bluff-body's downstream. Additionally, the region of greatest positive RI is observed near the combustor wall and the bluff-body's wake. This figure shows that the downstream region acts as a new source for driving thermoacoustic oscillations.

The observations of Rayleigh index distributions for the different cases of bluff bodies also match with the flame response, calculated as the amplitude of the dominant mode of local heat release rate fluctuations averaged in the radial direction and plotted as a function of the axial direction (refer Supplemental S1).

Conclusion

In this study, we analysed the results of a suppression strategy to reduce the growth of local heat release rate fluctuations to prevent the transition from combustion noise to thermoacoustic instability. Our experimental investigation suggests that certain configurations of perforations on the bluff-body ensures a reduction in the growth of local heat release rate fluctuations upstream of the bluff-body and hence aids in suppressing the onset of thermoacoustic instability. We observed that, in general, suppression of the onset of thermoacoustic instability is possible for such a passive control strategy. The success of this strategy shows that passive control can be designed based on the growth of local heat release rate fluctuations well before the occurrence of thermoacoustic instability.

However, the reduction in the amplitude of pressure oscillations is lower if the bluff-body is brought closer to the dump plane. The less effective suppression for this configuration using the IS bluff body shows the need to analyse the growth of local σ^2 when the bluff-body position is changed. Further, we need to have an optimisation strategy to find the appropriate area of passage with respect to the position of the bluff-body such that the growth of local heat release rate fluctuations can be reduced at the stagnation zone.

Most importantly, a mere introduction of slots on the bluff-body does not result in the suppression of the transition to thermoacoustic instability. We observed that the suppression of the transition to thermoacoustic instability does not occur if the area of the slots is lowered (4H bluff-body). We also found that an inappropriate distribution of the slots could result in a secondary bifurcation, leading to a catastrophic increase (300%) in the amplitudes of pressure oscillations (MH bluff-body). These results highlight the challenge of suppressing thermoacoustic instability in a spatially extended system, wherein many spatiotemporal patterns that result in the positive feedback between the acoustic pressure and heat release rate and thermoacoustic instability exist.

We emphasise that using different bluff-body designs was not to show the generalisation of the control strategy but instead, to prove the fact that effective suppression of the growth of heat release rate fluctuations at critical regions prevents thermoacoustic instability. Thus, the generalisation of

the control strategy is in (1) finding critical regions and (2) devising methods that can reduce the growth of local heat release rate fluctuations at critical regions and at the same time not initiate new critical regions. Instead of using slots, another possibility would be in using secondary air/fuel injections at these locations to modify the dynamics. Further, we hypothesise that analysis of the growth of local heat release rate fluctuations in swirl-stabilised flames, v-gutters and so on would reveal critical regions where control strategy can be implemented.

Acknowledgements

The authors would like to express their gratitude to Mr Midhun PR, Mr Anand S, and Mr Thilagaraj S of Aerospace department, IIT Madras for their assistance in conducting the experiments.

Declaration of Conflicting Interests

The author(s) declared no potential conflicts of interest with respect to the research, authorship, and/or publication of this article.

Funding

The author(s) disclosed receipt of the following financial support for the research, authorship, and/or publication of this article: This research is funded by the Science and Engineering Research Board (SERB) of the Department of Science and Technology (grant no: CRG/2020/003/051), Government of India and also by the IoE initiative (SB/2021/0845/AE/MHRD/002696), IIT Madras, India. NBG acknowledges the financial support of the East Africa Peru India Climate Capacities project (18_IL149_Global_A_Risikovorhersage) funded by the Federal Ministry for the Environment, Nature Conservation and Nuclear Safety and the International Climate Initiative.

ORCID iD

Manikandan Raghunathan  <https://orcid.org/0000-0003-3926-0072>

Supplemental material

Supplemental material for this article is available online.

References

1. Huang Y and Yang V. Dynamics and stability of lean-premixed swirl-stabilized combustion. *Prog Energy Combust Sci* 2009; 35: 293–364.
2. Juniper MP and Sujith RI. Sensitivity and nonlinearity of thermoacoustic oscillations. *Annu Rev Fluid Mech* 2018; 50: 661–689.
3. Nair V, Thampi G, Karuppusamy S, et al. Loss of chaos in combustion noise as a precursor of impending combustion instability. *Int J Spray Combust Dynam* 2013; 5: 273–290.
4. Tony J, Gopalakrishnan E, Sreelekha E, et al. Detecting deterministic nature of pressure measurements from a turbulent combustor. *Phys Rev E* 2015; 92: 062902.
5. Docquier N and Candel S. Combustion control and sensors: a review. *Prog Energy Combust Sci* 2002; 28: 107–150.

6. Schadow K and Gutmark E. Combustion instability related to vortex shedding in dump combustors and their passive control. *Prog Energy Combust Sci* 1992; 18: 117–132.
7. Paschereit CO, Gutmark E and Weisenstein W. Control of thermoacoustic instabilities and emissions in an industrial-type gas-turbine combustor. In: *Symposium (International) on Combustion*, volume 27. Elsevier, 1998, pp. 1817–1824.
8. LaBry ZA. *Suppression of thermoacoustic instabilities in a swirl combustor through microjet air injection*. PhD Thesis, Massachusetts Institute of Technology. 2010.
9. Schadow K, Gutmark E, Wilson K, et al. Multistep dump combustor design to reduce combustion instabilities. *J Propuls Power* 1990; 6: 407–411.
10. Lee JG, Kim K and Santavicca DA. Effect of injection location on the effectiveness of an active control system using secondary fuel injection. *Proc Combust Inst* 2000; 28: 739–746.
11. Altay HM, Hudgins DE, Speth RL, et al. Mitigation of thermoacoustic instability utilizing steady air injection near the flame anchoring zone. *Combust Flame* 2010; 157: 686–700.
12. Hussain T, Talibi M and Balachandran R. Investigating the effect of local addition of hydrogen to acoustically excited ethylene and methane flames. *Int J Hydrogen Energy* 2019; 44: 11168–11184.
13. Aguilar JG and Juniper MP. Thermoacoustic stabilization of a longitudinal combustor using adjoint methods. *Phys Rev Fluids* 2020; 5: 083902.
14. Tammissola O and Juniper MP. Coherent structures in a swirl injector at $Re = 4800$ by nonlinear simulations and linear global modes. *J Fluid Mech* 2016; 792: 620–657.
15. Schadow K, Gutmark E, Parr T, et al. Large-scale coherent structures as drivers of combustion instability. *Combust Sci Technol* 1989; 64: 167–186.
16. Paschereit CO, Gutmark E and Weisenstein W. Structure and control of thermoacoustic instabilities in a gas-turbine combustor. *Combust Sci Technol* 1998; 138: 213–232.
17. Premchand CP, Raghunathan M, Midhun PR, et al. Smart passive control of thermoacoustic instability in a bluff-body stabilized combustor: a Lagrangian analysis of critical structures. In: *Turbo Expo: Power for Land, Sea, and Air*, volume 84133. American Society of Mechanical Engineers, p. V04BT04A040, 2020.
18. Lieuwen TC. Experimental investigation of limit-cycle oscillations in an unstable gas turbine combustor. *J Propuls Power* 2002; 18: 61–67.
19. Nair V, Thampi G and Sujith RI. Intermittency route to thermoacoustic instability in turbulent combustors. *J Fluid Mech* 2014; 756: 470–487.
20. Mondal S, Unni VR and Sujith RI. Onset of thermoacoustic instability in turbulent combustors: an emergence of synchronized periodicity through formation of chimera-like states. *J Fluid Mech* 2017; 811: 659–681.
21. George NB, Unni VR, Raghunathan M, et al. Pattern formation during transition from combustion noise to thermoacoustic instability via intermittency. *J Fluid Mech* 2018; 849: 615–644.
22. Raghunathan M, George NB, Unni VR, et al. Multifractal analysis of flame dynamics during transition to thermoacoustic instability in a turbulent combustor. *J Fluid Mech* 2020; 888.
23. Gotoda H, Shinoda Y, Kobayashi M, et al. Detection and control of combustion instability based on the concept of dynamical system theory. *Phys Rev E* 2014; 89: 022910.
24. Nair V and Sujith RI. Multifractality in combustion noise: predicting an impending combustion instability. *J Fluid Mech* 2014; 747: 635–655.
25. Nair V, Thampi G and Sujith RI. Engineering precursors to forewarn the onset of an impending combustion instability. In: *Turbo Expo: Power for Land, Sea, and Air*, volume 45691. American Society of Mechanical Engineers, p. V04BT04A005; 2014.
26. Gopalakrishnan EA, Sharma Y, John T, et al. Early warning signals for critical transitions in a thermoacoustic system. *Sci Rep* 2016; 6: 1–10.
27. Pavithran I, Unni VR and Sujith RI. Critical transitions and their early warning signals in thermoacoustic systems. *Eur Phys J Spec Top* 2021; 230: 3411–3432.
28. Hashimoto T, Shibuya H, Gotoda H, et al. Spatiotemporal dynamics and early detection of thermoacoustic combustion instability in a model rocket combustor. *Phys Rev E* 2019; 99: 032208.
29. Kobayashi T, Murayama S, Hachijo T, et al. Early detection of thermoacoustic combustion instability using a methodology combining complex networks and machine learning. *Phys Rev Appl* 2019; 11: 064034.
30. Lee M, Kim KT, Gupta V, et al. System identification and early warning detection of thermoacoustic oscillations in a turbulent combustor using its noise-induced dynamics. *Proc Combust Inst* 2021; 38: 6025–6033.
31. Wu W and Wang J. Generalized fluctuation-dissipation theorem for non-equilibrium spatially extended systems. *Front Phys* 2020; 8: 567523.
32. Getling A. *Rayleigh-Bénard Convection: Structures and Dynamics*. Advanced series in nonlinear dynamics. World Scientific; 1998. ISBN 9789810226572. doi: 10.1142/3097.
33. Mukutmoni D and Yang K. Flow transitions and pattern selection of the Rayleigh-Bénard problem in rectangular enclosures. *Sadhana* 1994; 19: 649–670.
34. Pandey A, Scheel JD and Schumacher J. Turbulent superstructures in Rayleigh-Bénard convection. *Nat Commun* 2018; 9: 1–11.
35. Parekh N and Sinha S. Controllability of spatiotemporal systems using constant pinnings. *Phys A: Stat Mech Appl* 2003; 318: 200–212.
36. George NB, Raghunathan M, Unni VR, et al. Preventing a global transition to thermoacoustic instability by targeting local dynamics. *Sci Rep* 2022; 12: 1–11.
37. Raghunathan M, George NB, Unni VR, et al. Seeds of phase transition to thermoacoustic instability. *New J Phys* 2022; 24: 063008.
38. Scheffer M, Carpenter S, Foley JA, et al. Catastrophic shifts in ecosystems. *Nature* 2001; 413: 591–596.
39. Yang H, Shew WL, Roy R, et al. Maximal variability of phase synchrony in cortical networks with neuronal avalanches. *J Neurosci* 2012; 32: 1061–1072.
40. Kanders K, Lee H, Hong N, et al. Fingerprints of a second order critical line in developing neural networks. *Commun Phys* 2020; 3: 1–13.
41. Pawar SA, Seshadri A, Unni VR, et al. Thermoacoustic instability as mutual synchronization between the acoustic

- field of the confinement and turbulent reactive flow. *J Fluid Mech* 2017; 827: 664–693.
42. Stöhr M, Sadanandan R and Meier W. Experimental study of unsteady flame structures of an oscillating swirl flame in a gas turbine model combustor. *Proc Combust Inst* 2009; 32: 2925–2932.
 43. Steinberg AM, Boxx I, Stöhr M, et al. Flow–flame interactions causing acoustically coupled heat release fluctuations in a thermo-acoustically unstable gas turbine model combustor. *Combust Flame* 2010; 157: 2250–2266.
 44. Landau L and Lifshitz E. *Course of theoretical physics*. Pergamon: Elsevier, 2013.
 45. Surovyatkina E, Kravtsov YA and Kurths J. Fluctuation growth and saturation in nonlinear oscillators on the threshold of bifurcation of spontaneous symmetry breaking. *Phys Rev E* 2005; 72: 046125.
 46. Roy A, Singh S, Nair A, et al. Flame dynamics during intermittency and secondary bifurcation to longitudinal thermoacoustic instability in a swirl-stabilized annular combustor. *Proc Combust Inst* 2021; 38: 6221–6230.
 47. Ananthkrishnan N, Sudhakar K, Sudershan S, et al. Application of secondary bifurcations to large-amplitude limit cycles in mechanical systems. *J Sound Vib* 1998; 215: 183–188.
 48. Lee J and Santavicca D. Experimental diagnostics for the study of combustion instabilities in lean premixed combustors. *J Propuls Power* 2003; 19: 735–750.